Experimental Evaluation of Mechanical Compression Properties of Aluminum Alloy Lattice Trusses for Anti-Ice System Applications

machines

MDPI

Article

Experimental Evaluation of Mechanical Compression Properties of Aluminum Alloy Lattice Trusses for Anti-Ice System Applications

Carlo Giovanni Ferro [1,*], Sara Varetti [1,2] and Paolo Maggiore [1]

[1] Department of Mechanical and Aerospace Engineering, Politecnico di Torino, Corso Duca degli Abruzzi, 10124 Torino, Italy; sara.varetti@leonardo.com (S.V.); paolo.maggiore@polito.it (P.M.)
[2] Leonardo Labs, 74023 Grottaglie, Italy
* Correspondence: carlo.ferro@polito.it

Abstract: Lattice structures have emerged as promising materials for aerospace structure applications due to their high strength-to-weight ratios, customizable properties, and efficient use of materials. These properties make them attractive for use in anti-ice systems, where lightweight and heat exchange are essential. This paper presents an extensive experimental investigation into mechanical compression properties of lattice trusses fabricated from AlSi10Mg powder alloy, a material commonly used in casted aerospace parts. The truss structures were manufactured using the additive manufacturing selective laser melting technique and were subjected to uniaxial compressive loading to assess their performance. The results demonstrate that AlSi10Mg lattice trusses exhibit remarkable compressive strength with strong correlations depending upon both topology and cells' parameters setup. The findings described highlight the potential of AlSi10Mg alloy as a promising material for custom truss fabrication, offering customizable cost-effective and lightweight solutions for the aerospace market. This study also emphasizes the role of additive manufacturing in producing complex structures with pointwise-tailored mechanical properties.

Keywords: additive manufacturing (AM); selective laser melting (SLM); lattice structures; design of experiments (DOE)

Citation: Ferro, C.G.; Varetti, S.; Maggiore, P. Experimental Evaluation of Mechanical Compression Properties of Aluminum Alloy Lattice Trusses for Anti-Ice System Applications. *Machines* **2024**, *12*, 404. https://doi.org/10.3390/machines12060404

Academic Editor: Kai Cheng

Received: 23 April 2024
Revised: 19 May 2024
Accepted: 31 May 2024
Published: 12 June 2024

1. Introduction

The aviation industry is under increasing pressure to reduce its carbon footprint due to the significant contribution to global greenhouse gas emissions [1–7]. With the projected growth in air travel, the demand for more fuel-efficient and environmentally friendly aircrafts is becoming a priority for manufacturers. One way to achieve this goal is by empowering global fuel to improve efficiency through the introduction of novel technologies such as additive manufacturing (AM) [8]. AM offers significant benefits to the aerospace industry, including reduced material waste, increased design flexibility, and faster production times [9]. The use of AM in aerospace products has the potential to significantly reduce the carbon footprint of aviation while also improving performance and reducing costs [10–15].

The proposed work presents a novel anti-ice system completely redesigned to substitute the classic hot air leading edge anti-icing system for liner aircrafts [16]. The introduction of AM permits obtaining a single-piece sandwich panel in which the internal lattice acts simultaneously as heat exchanger and structural core [17,18]. Both solution schematics are presented in Figure 1.

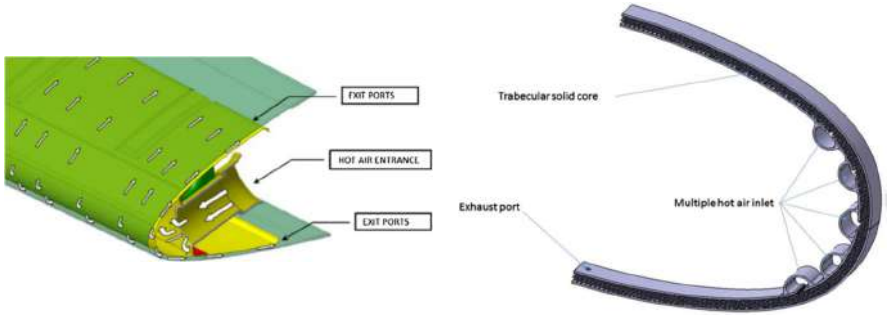

(**a**) (**b**)

Figure 1. Anti-icing system: (**a**) traditional thermal anti-icing system [19], (**b**) Novel Integrated Anti Ice Panel [20].

On an industry level case-study this patented solution has proven to reach a sensible weight reduction (−46%), a unification into a single piece with reduced maintenance cost and a better heat exchange performance that could lead to a reduction of the spilled mass flow of the 30% with fuel savings [21]. This achievement is obtainable only by shifting towards modern manufacturing technology such as SLM (selective laser melting) which permits creating single piece complex geometries.

The present evaluation of mechanical compression properties of lattice trusses made with AlSi10Mg for an anti-ice system is one part of a broader design project involving several other studies and tests such as fatigue analysis and CFD simulations [20,22–24].

The exploration of lattice structures has been a significant topic in materials science and engineering, with comprehensive studies delving into various aspects of their mechanical properties [11,15,18,25–30]. Previous literature has extensively studied linear elasticity properties, under different loading conditions such as tension/compression and bending [31–33].

The advancements in additive manufacturing technologies have further propelled the development and utilization of lattice structures, allowing for complex designs that were previously unattainable through traditional manufacturing methods. However, the design and analysis of lattice structures necessitate a comprehensive understanding of their mechanical behavior [34,35]. The homogenization method plays a pivotal role in the design and analysis of those trusses by providing a means to derive effective macroscopic properties from the unit cell behavior [36,37]. This method involves averaging the mechanical properties over a representative volume element (RVE) to obtain equivalent continuum properties, thereby simplifying the analysis of complex lattice geometries [38–44]. Homogenization techniques are particularly beneficial in the early stages of design, where they enable efficient optimization and performance prediction without resorting to computationally expensive full-scale simulations.

2. Materials and Methods

In the current study, an experimental approach was implemented, which considered different cell features and a statistical analysis for a bird's-eye exploration of the structure–property relationships in lattices. The focus is on aluminum alloy AlSi10Mg, chosen for its printability in SLM machines and for its bulk mechanical properties suitable for applications in anti-icing systems.

Regarding the the specimens designed for compression tests, the shapes produced were parallelepipeds measuring $20 \times 20 \times 40$ mm. Although the height selection introduced a shear buckling effect on some single cell failure, it was decided to maintain the specimens' size in line with previous studies [17] in order to permit direct comparisons between experimental cells. The dimensions of each specimen slightly varied based on cell sizes to ensure a finite number of cells on each side. The shape of the specimens, being twice as

tall as the base's side, facilitated the examination of fracture behavior in various trabecular structures intended for the core of sandwich panels, minimizing the corner/edge effects.

A full factorial design (FFD) [45,46] with three variables and three values for each variable was developed; the analysis is graphically shown in Figure 2. Three parameters were selected for the experiment: cell type (shapes reported in Appendix A), cell size, and relative density. For cell type, three shapes were selected: Bccz (a stretching dominated structure) and two bending types, octet truss and rhombic dodecahedron. The second parameter chosen was the cell size which determines the length of the cell's sides (with all cells being cubic). The last parameter chosen was the relative density parameter which indicates the density of the elementary cells relative to the filled cube of the reference cell. Numerical data related to these parameters and the design approach are outlined in Table 1.

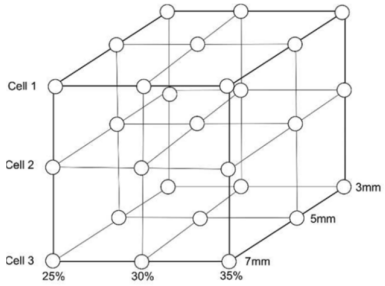

Figure 2. DOE full factorial design.

Table 1. Truss cells DOE design.

Cell Type	Cell Size [mm]	Volume Fraction [%]
Bccz	3	30
Bccz	5	25
Bccz	7	35
Rhombic	3	25
Rhombic	5	35
Rhombic	7	30
Octet	3	35
Octet	5	30
Octet	7	25

Lattices were fabricated utilizing an SLM 500 (Beamit of Parma, Parma, Italy) machine system [47]. This AM technique uses a high-power laser to sinter metal particles into a three-dimensional configuration. The process initiates with the laser selectively melting a layer of powdered material according to a predetermined 3D digital design. After each melting session, the powder bed is lowered, and a fresh layer of powder is spread. This procedure is iteratively executed, enabling the production of detailed and high-fidelity lattice structures. All specimens were printed with an SLM500 machine, with a laser power of 350 W, a scanning speed of 1500 mm/s and a layer thickness of 50 µm.

The SLM 500 machine permits the creation of metal components with notable mechanical attributes, intricate geometries, precise dimensions, and superior surface quality. Its incorporation of a quadruple laser system ensures rapid construction rates and efficient fabrication of large-scale components, suitable for aircraft's leading edges. For this study, the SLM 500's capabilities were leveraged to manufacture AlSi10Mg lattice trusses.

Compression testing was performed using a Zwick Roell testing machine equipped with a 50 kN load cell. The tests were executed at a constant speed of 1 mm/min, applying a pre-load of 1 kN. Figure 3 illustrates the machine's setup for the uniaxial compression tests.

Each specimen is described in the results section, identified by a label summarizing the cell's shape, size, and theoretical volume fraction. For example, the specimen labeled

"Rhombic-5-25-2" features a rhombic dodecahedron geometry, a cell size of 5 mm, and a solid volume fraction of 25%. The final number in each specimen's label indicates the sequence of repetition, with this particular sample being the second in its series.

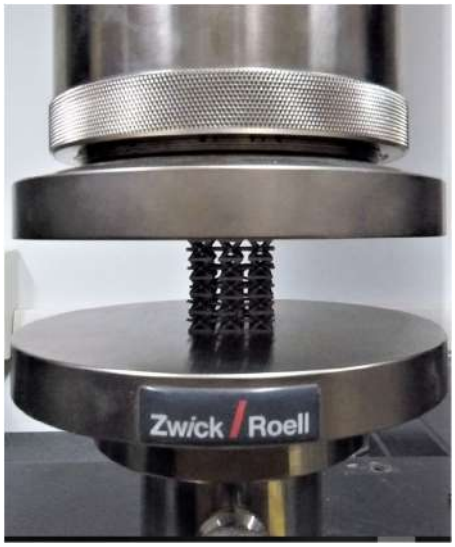

Figure 3. Setup of the Zwick Roell machine for uniaxial compression test on trabecular specimens.

The compression tests were analyzed using three distinct metrics derived from the stress–strain curves:

- Lattice equivalent Young's Modulus (E), calculated from the slope of the stress–strain curve obtained by the compression of the lattices within the linear elastic region;
- Maximum Stress (σ_{max}), representing the highest point on the curve compression/deformation of the lattices;
- Yield Stress ($\sigma_{0.2}$), defined as the lattice stress value corresponding to a permanent plastic deformation of 0.2%.

The value of $\sigma_{0.2}$ is particularly significant as it marks the onset of the lattice's plastic deformation phase. This is determined by evaluating a parallel linear trend to the initial linear elastic portion of the specimen's behavior, intersecting at a deformation of 0.2%. Considering the variability in specimen dimensions, the main compressive property values are also normalized and presented in Appendix B.

3. Results

This section presents and discusses the experimental results obtained from the lattices compression test. It includes both a quantitative report of the findings and a qualitative analysis of the rupture mechanisms observed. Detailed data on these outcomes is available in Appendix B.

3.1. Bccz Specimens

Stress–strain behaviors for Bccz specimens are presented in Figure 4. Notably, specimen 3_35 achieved the highest maximum stress of 149 MPa, showing significant plastic deformation with a strain at break reaching 15%. In contrast, Specimen 7_25, while registering the lowest σ_{max} among the tested specimens, 32 MPa, also exhibited minimal plastic deformation, not exceeding a 10% strain at break. Preliminary analysis indicates a predominant influence of cell size on the σ values, observing a decrement in mechanical performance from cell sizes 3 to 5 mm and subsequent stabilization moving from 5 to 7 mm cells.

Additionally, a consistent upward trend is observed across the increase of relative density in enhancing also Young's modulus: in fact, if a cell size of 5 mm is taken as

reference, the 25% relative density exhibits a medium Young's modulus of 1322 MPa while 30% presents a medium value of 1579 MPa and 35% a peak value of 2011 MPa. This relationship highlights the critical role of density in determining the material's mechanical characteristics. This aligns with the Gibson–Ashby model, which correlates an increase in relative density with enhanced mechanical properties.

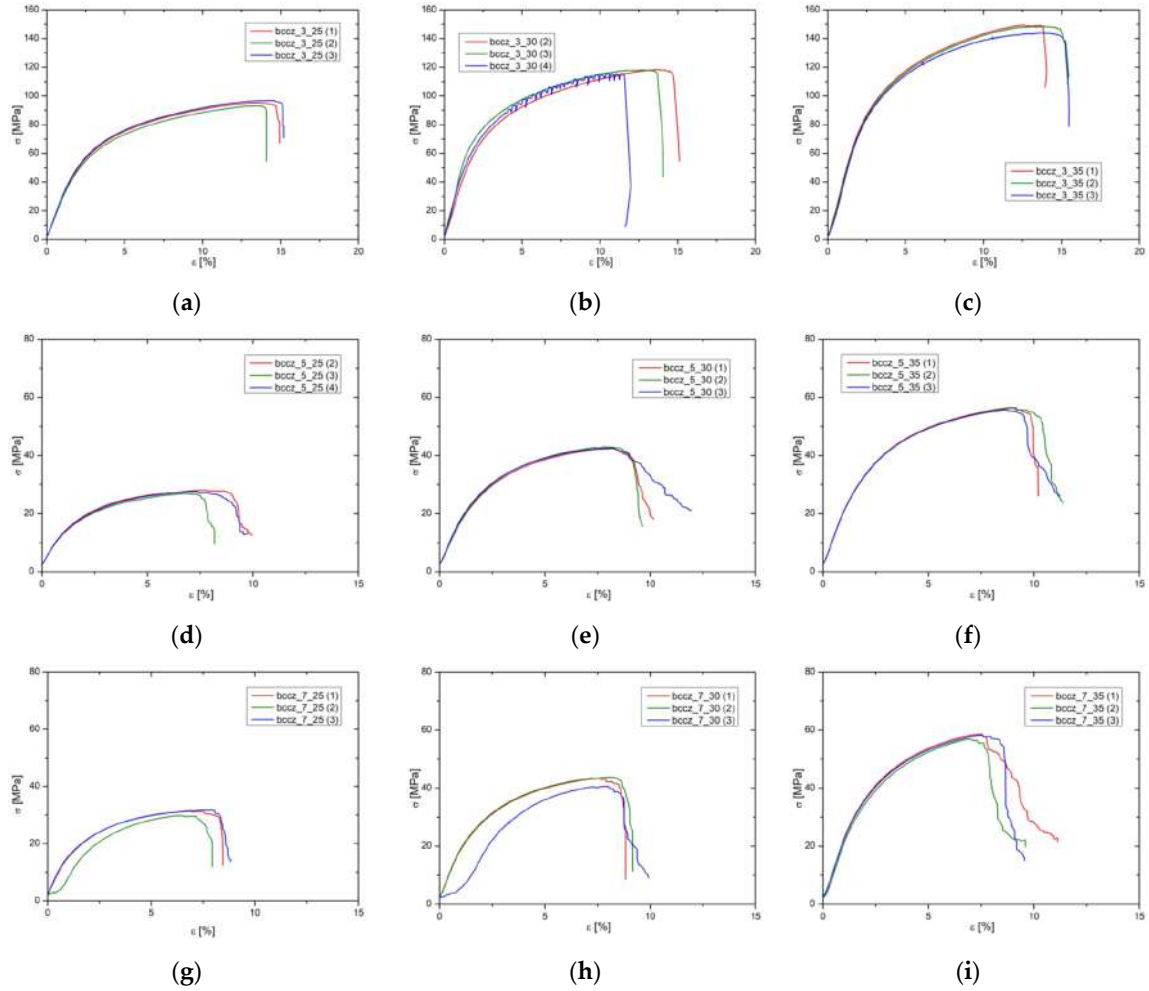

Figure 4. Stress–strain curves for Bccz specimens: (**a**) 3 mm cells 25% density, (**b**) 3 mm cells 30% density, (**c**) 3 mm cells 35% density, (**d**) 5 mm cells 25% density, (**e**) 5 mm cells 30% density, (**f**) 5 mm cells 35% density, (**g**) 7 mm cells 25% density, (**h**) 7 mm cells 30% density, (**i**) 7 mm cells 35% density.

In mechanical failure of BCCZ trabecular structures, the initial collapse typically originates from buckling in the vertical struts, initiating on one side of the specimen approximately at mid-height. This leads to the subsequent failure of a trabecular plane, inclined at 45 degrees to the Z-axis, evident as a marked decrease in resistance on stress–strain curves. Post-initial failure, the specimen exhibits increased resistance, attributed to the stabilization of adjacent cell planes compressed together. The second failure phase, occurring at lower loads than the first, varies with cell size but appears independent of the solid volume fraction. This behavior is observed in Figure 5. while broken post-test specimens are shown in Figure 6.

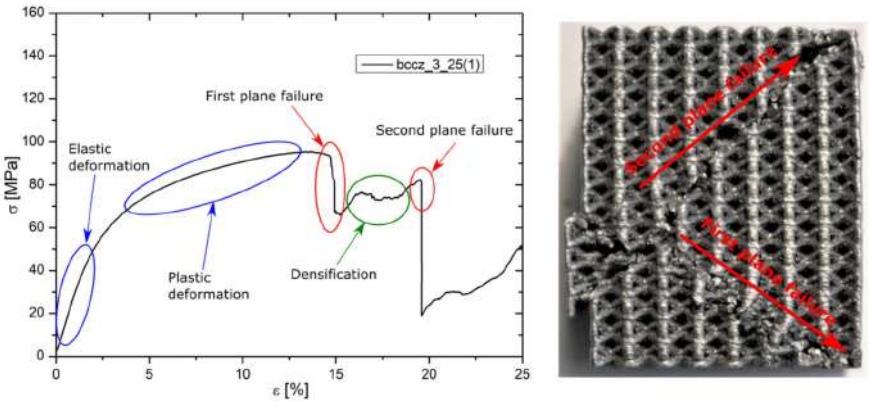

Figure 5. Phases of the compression test on Bccz-3-25-1 specimen.

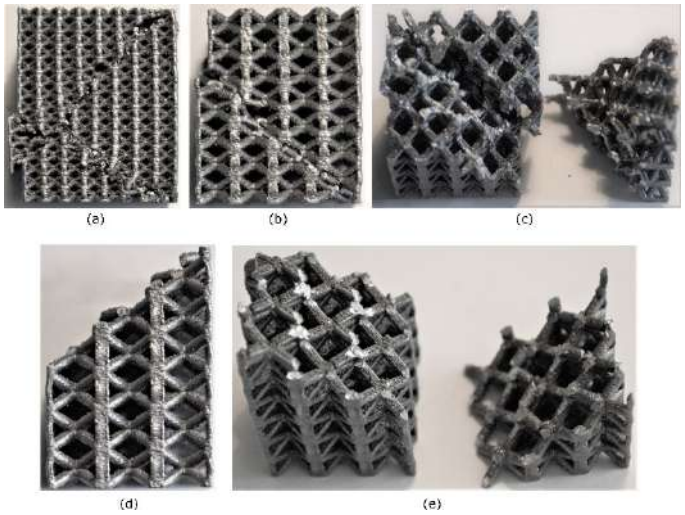

Figure 6. Tested specimens in different conditions: (**a**) Bccz-3-25-1 after the failure of the second plane, (**b**) Bccz-5-30-2 after the failure of the first plane, (**c**) Bccz-5-35-1 continuing the test after the failure of the first plane, (**d**) Bccz-7-25-1 after the failure of the first plane and (**e**) Bccz-7-30-2 after the failure of the first plane. Tested specimens: (**a**) Bccz-3-30-3, (**b**) Bccz-5-25-2 and (**c**) Bccz-7-35-1.

3.2. Rhombic Dodecahedron Specimens

Figure 7 denotes the stress–strain relationships for specimens with rhombic dodecahedron cell structures. These rhombic cells, across varying sizes, demonstrate reduced deformation prior to reaching the point of failure compared to BCCZ, with failure occurring at approximately 7% strain in contrast to the 13% observed before. Comparative analysis of these curves reveals that an increase in solid volume fraction is associated with linear improved mechanical performance; also, a similar enhancement in mechanical properties is observed with the decreasing of cell size from 7 to 3 mm, albeit in a less linear fashion. In terms of trends for maximum stress (σ_{max}), yield stress (σ_{02}), and Young's modulus (E), the results are consistent with those observed in Bccz and Octet-truss specimens. However, the absolute values are lower for the rhombic dodecahedron specimens, attributable to their distinct failure mechanism, which is bending-dominated rather than stretching-dominated (bccz).

The specimens featuring rhombic dodecahedron cell geometry exhibit a distinct failure mechanism compared to the Bccz specimens. In rhombic specimens, failure consistently results from strut fractures at the nodes. This occurs as compression forces concentrate stresses where struts converge. The oblique struts gradually draw closer until they fracture at the node. Failure manifests through the collapse of a plane oriented at a 45-degree angle relative to the Z-axis. Notably, this collapse initiates from the specimen's corner, contrasting

with the Bccz specimens where failure typically originates from one side. Figure 8 illustrates this phenomenon, displaying several rhombic specimens at different stages of breakage during the compression tests, highlighting the variation in cell size.

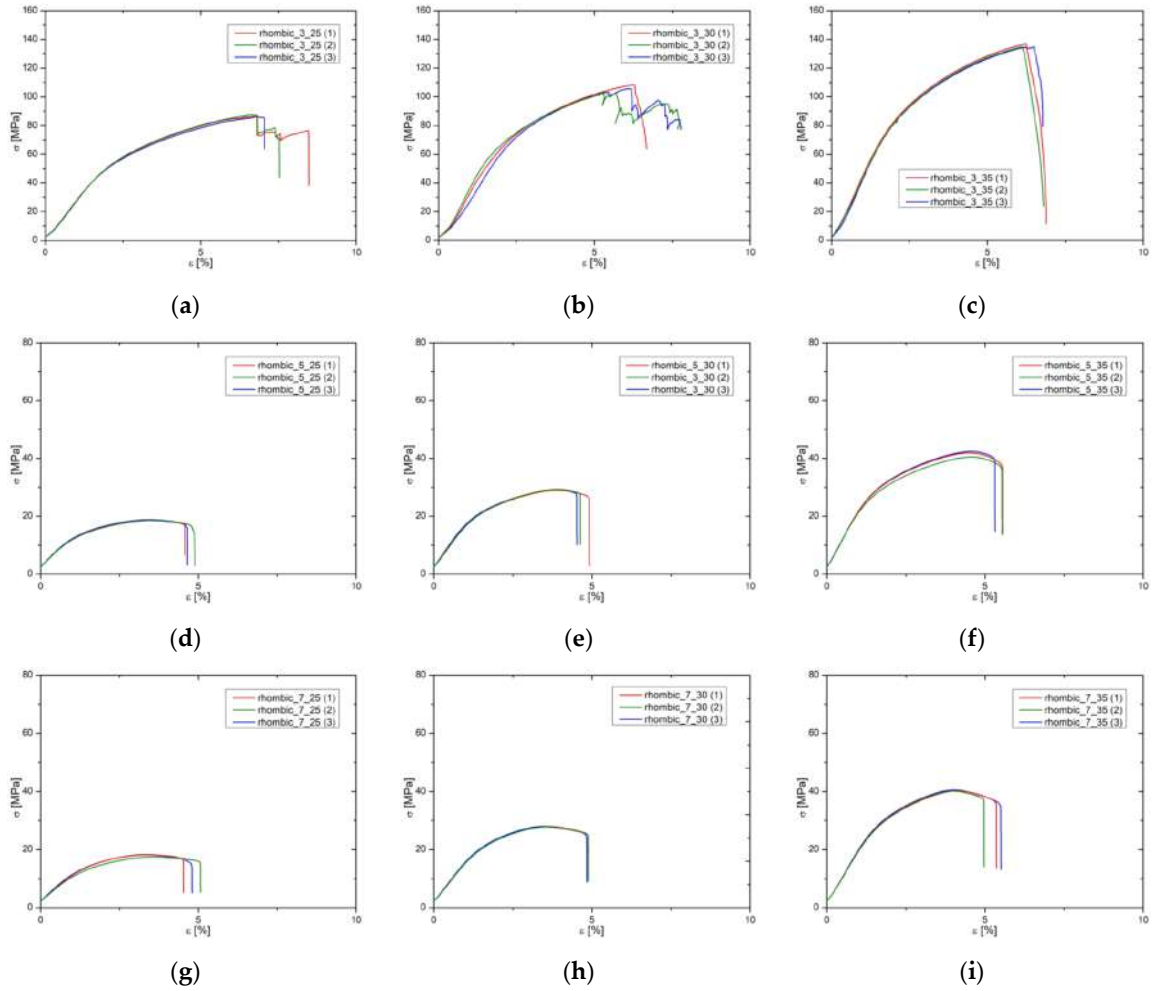

Figure 7. Stress–strain curves for rhombic dodecahedron specimens: (**a**) 3 mm cells 25% density, (**b**) 3 mm cells 30% density, (**c**) 3 mm cells 35% density, (**d**) 5 mm cells 25% density, (**e**) 5 mm cells 30% density, (**f**) 5 mm cells 35% density, (**g**) 7mm cells 25% density, (**h**) 7 mm cells 30% density, (**i**) 7 mm cells 35% density.

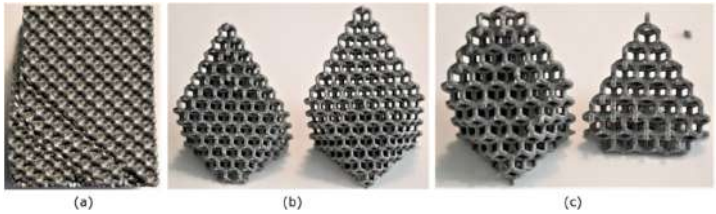

Figure 8. Tested specimens in different conditions: (**a**) Rhom-3-25-1 after the failure of the second plane, (**b**) Rhom-5-25-1 after the failure of the first plane and (**c**) Rhom-7-30-2 after the failure of the first plane.

3.3. Octet-Truss Specimens

In the experimental evaluation of octet-truss structures, the 3 mm cell size specimens distinctly exhibited superior mechanical properties, characterized by the highest stresses at rupture, yield stress, and at Young's modulus, as shown in Figure 9. These graphs also

underscore the positive impact of augmentation of relative density on the enhancement of mechanical properties in these structures. Comparatively, for what concerns cell size, 5 and 7 mm demonstrated lower mechanical stress–strain responses compared to 3 mm cells. Their behavior of bigger cells resembles that of a traditional truss structure, in contrast to the 3 mm specimens which manifested characteristics akin to a porous solid. Notably, the strain levels for all specimens remained consistently below 10%, further distinguishing their mechanical response of bending trusses compared to stretching ones.

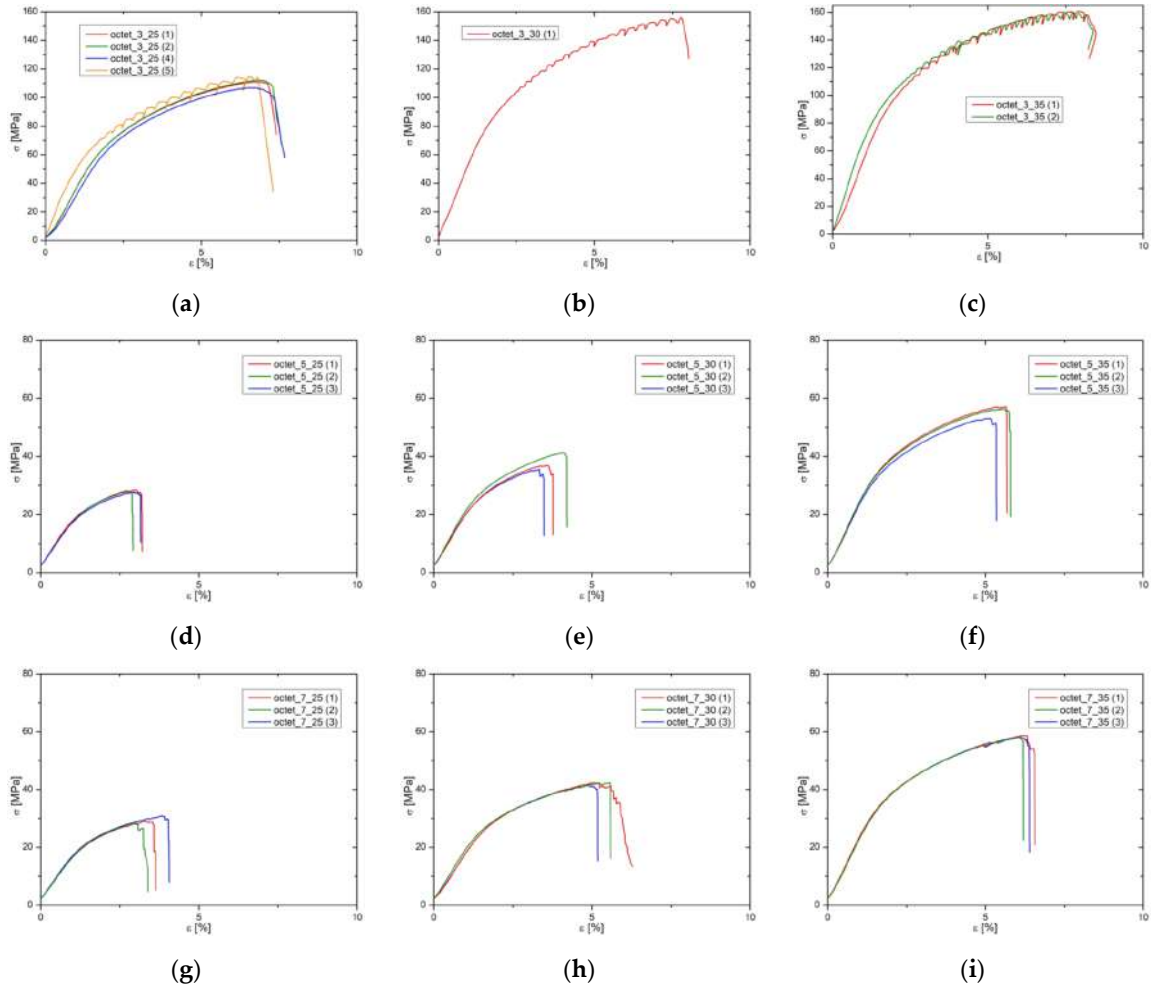

Figure 9. Stress–strain curves for octet-truss specimens: (**a**) 3 mm cells 25% density, (**b**) 3 mm cells 30% density, (**c**) 3 mm cells 35% density, (**d**) 5 mm cells 25% density, (**e**) 5 mm cells 30% density, (**f**) 5 mm cells 35% density, (**g**) 7 mm cells 25% density, (**h**) 7 mm cells 30% density, (**i**) 7 mm cells 35% density.

The mechanical response at the point of fracture for structures with octet-truss cell geometry closely mirrors that of rhombic dodecahedron cells, albeit under higher load conditions. Similar to rhombic cells, failure in octet-truss structures predominantly results from strut fractures at the nodes, as noted in reference [48]. As shown from Figure 10 the failure pattern arises from stress concentrations at the nodes under compression loads, leading to the gradual convergence and eventual breakage of oblique struts at these points. This observation aligns with the behavior noted in rhombic cells, particularly in 3 mm octet cells, which demonstrate a distinct response compared to their 5 and 7 mm counterparts. Post-initial plane failure, adjacent planes start to fail, resulting in the densification of the specimen. The collapse of these structures tends to be abrupt and noisy, occasionally leading to a violent separation of the parts.

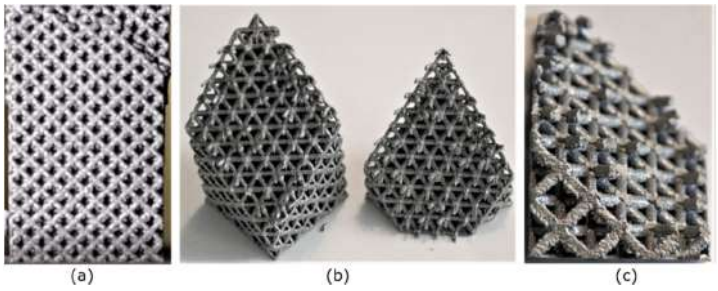

Figure 10. Tested specimens: (**a**) Oct-3-35-1, (**b**) Oct-5-30-2 and (**c**) Oct-7-25-3.

4. Discussion

In the following section, an analysis and comparison of the data presented in the Results section is conducted. This analysis aims to elucidate the impact of design parameters, thereby yielding novel insights into their influence.

4.1. DOE Analysis

Observing the DOE Pareto analysis' results reported in Figure 11, it is possible to elaborate some inferences. Firstly, the Pareto chart, encompassing various responses such as Young's modulus, maximum stress, and yield stress, indicates that all the DOE design parameters chosen significantly influenced these metrics. Cell size is the predominant parameter on both Young's modulus and yield stress while cell type influences mostly maximum stress. Relative density plays the less influential role in maximum stress while it is the second most important parameter in Young's modulus and yield stress.

Figure 12 reports main effects analysis; those graphs refer to the impact of individual factors on the response variables, without considering interactions between factors. The analysis of those outputs indicates that the octet lattice structure outperforms the other two cell types across all selected metrics, likely due to its shorter beam length. In contrast, the rhombic lattice, primarily influenced by bending behavior with slender beams, demonstrates inferior performance in maximum stress and Young's modulus compared to both BCCZ and octet structures. However, it surpasses the BCCZ structure in terms of yield stress. Additionally, an increase in relative density almost linearly enhances all evaluated metrics.

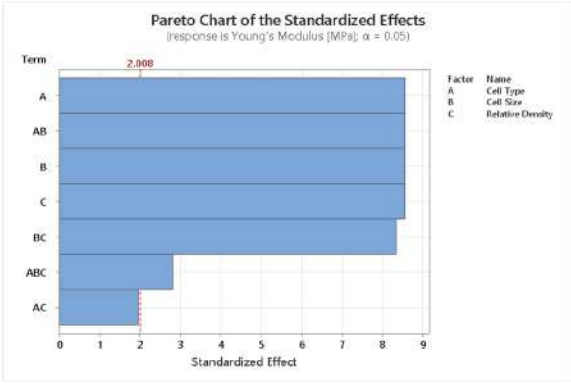

(**a**)

Figure 11. *Cont.*

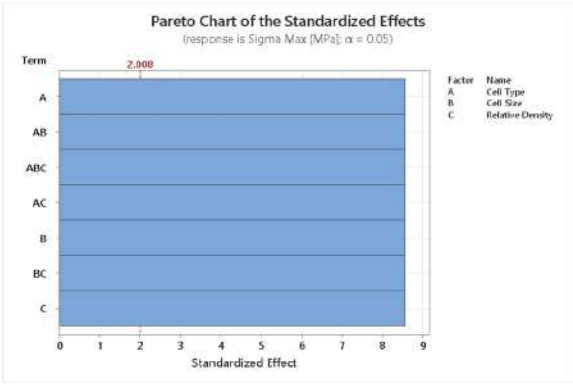

(**b**)

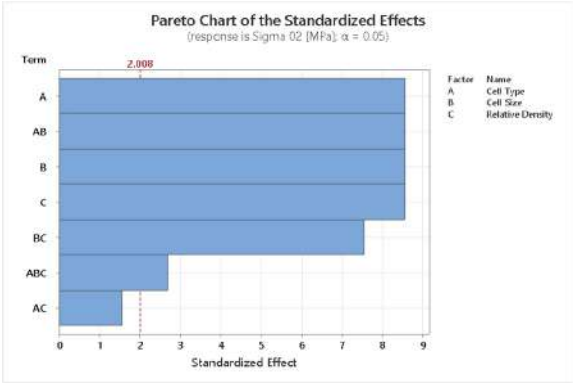

(**c**)

Figure 11. Pareto chart analysis: (**a**) graph for Young's Modulus, (**b**) graph for sigma max and (**c**) graph for Yield Stress.

Surface response behaviors, detailed in Figure 13, exhibit same non-linear characteristics reported in the main effects analysis helping in the complexity to identify optimal configurations. The residual plots, reported in Appendix B, demonstrate a satisfactory normal distribution, indicating errors distributed randomly in order of tests and fits, which suggests minimal systematic errors across all metrics.

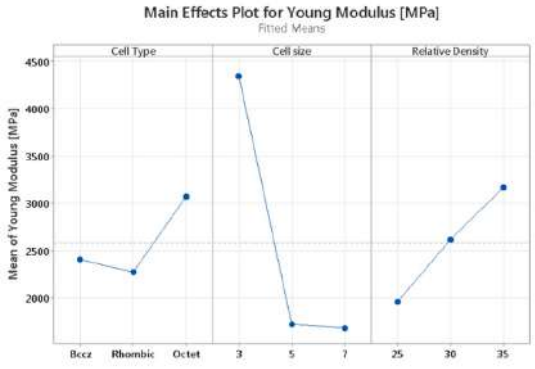

(**a**)

Figure 12. *Cont.*

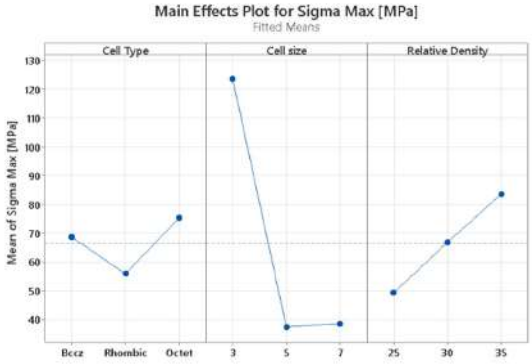

(**b**)

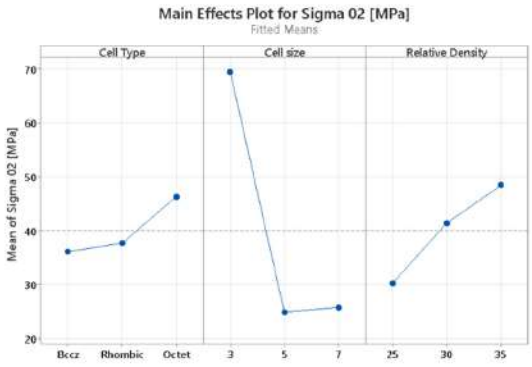

(**c**)

Figure 12. Main effects analysis: (**a**)Young Modulus, (**b**) Sigma Max [MPa], (**c**) Yield Stress [MPa].

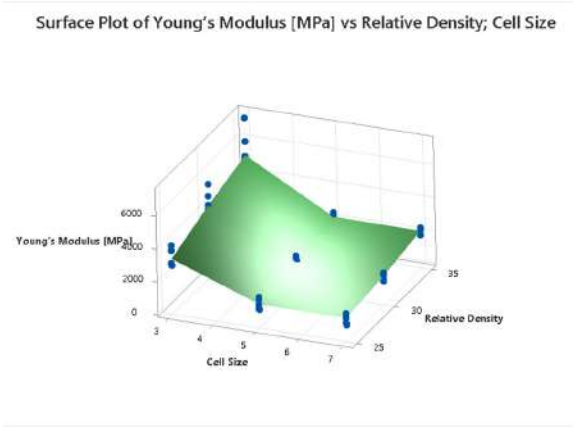

(**a**)

Figure 13. *Cont*.

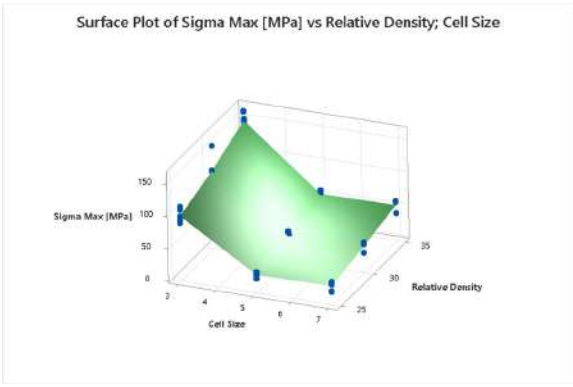

(**b**)

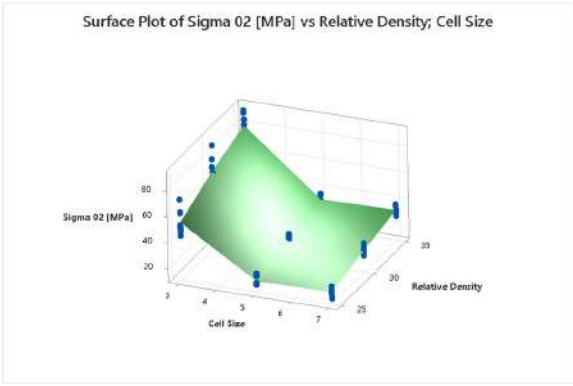

(**c**)

Figure 13. Surface plot: (**a**) Young's Modulus vs Cell Size and Relative Density, (**b**) Maximum Stress vs Cell Size and Density, (**c**) Yield Stress vs Cell Size and Density.

4.2. Comparison with Gibson–Ashby Model

The experimental data obtained for all the three cell geometries were compared with the Gibson–Ashby model for the foam with open cells. This model permits calculation of maximum strength and Young's modulus of the trabecular specimens, using the density and the mechanical values of the foam and of the correspondent dense material. According to the Gibson–Ashby model, mechanical characteristics of the foam are reported as relative values with respect to the quantities of the equivalent bulk solid. The relative density, the compressive modulus and the compressive strength are calculated respectively using the equations:

$$\rho = \rho_f / \rho_s \tag{1}$$

$$\frac{E_f}{E_s} = C_1 \left(\frac{\rho_f}{\rho_s} \right)^2 \tag{2}$$

$$\frac{\sigma_f}{\sigma_s} = C_2 \left(\frac{\rho_f}{\rho_s} \right)^{1.5} \tag{3}$$

where ρ is the relative density, ρ_f is the density of the foam, ρ_s of the solid, E_f is Young's modulus of the foam, E_s is Young's modulus of the solid, σ_f is the compressive strength of the foam, σ_s is the compressive strength of the solid, and C_1 and C_2 are specific constants that include all the geometric features of proportionality.

The mechanical values and properties of the fully dense AlSi10Mg alloy components were taken from EOS Datasheet [49]: the value of compressive σ_{max} is equal to 392 MPa, E is 72.4 GPa and ρ is 2.67 kg/dm^3.

Figure 14 provides a comparative analysis between experimental outcomes and predictions made by the Gibson–Ashby (GA) model for Bccz, octet, and rhombic specimens.

In detail, Figure 14a depicts the maximum stress (σ_{max}) results, where the GA model's predictions are represented by lines and the experimental data by points. It is observed that for specimens with lower density, the GA model aligns well with the experimental findings. However, as the density increases, the model's predictive accuracy diminishes.

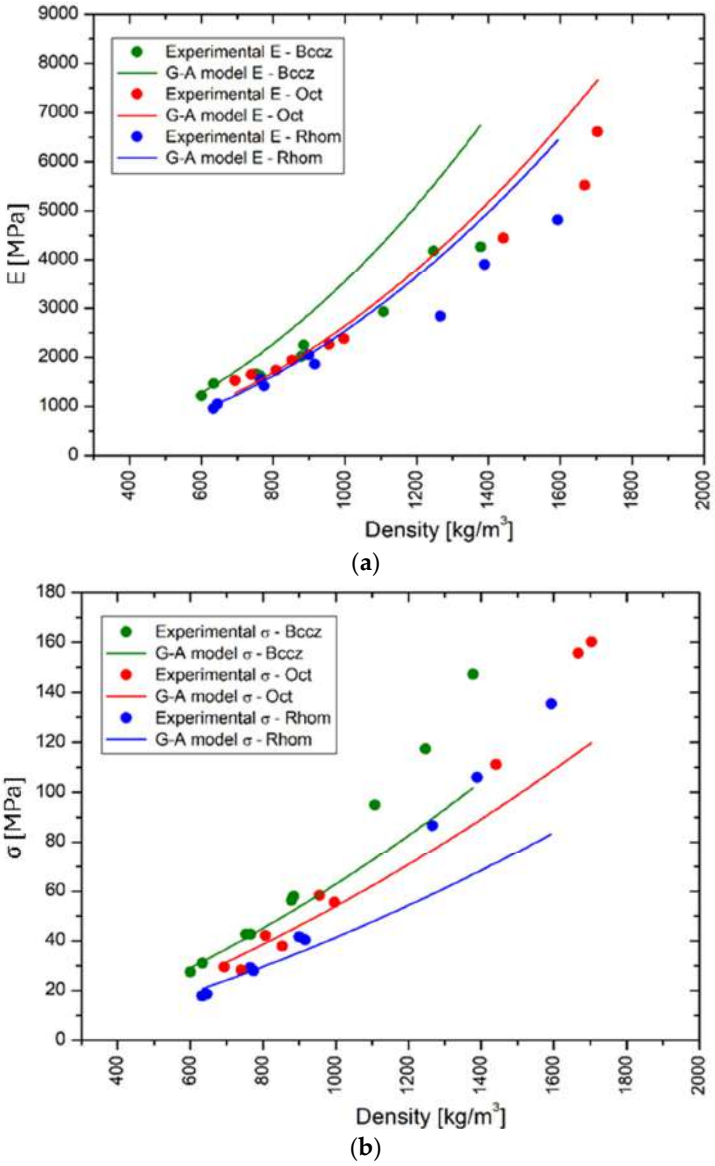

Figure 14. Comparison between experimental data for Bccz, octet and rhombic cells in AlSi10Mg with the values obtained from the Gibson–Ashby model for the same cells in terms of (**a**) σmax and (**b**) E.

This deviation could be attributed to design and manufacturing factors. From a design perspective, the GA model is primarily tailored for low-density foam materials, leading to challenges in accurately predicting the behavior of high-density trabecular structures.

On the manufacturing front, the discrepancy is particularly notable in specimens with 3 mm cell size. Optical Microscope (OM) analysis revealed an effective dimensional increase, likely caused by the coalescence of surrounding powder during the melting phase. As example of a comparative image for an octet 3 mm cell is shown in Figure 15. Moreover, X-ray tomography was conducted on trabecular specimens to visualize the internal structure of the struts. Figure 16 presents a comparison of different sections on XY planes of Bccz specimens produced from AlSi10Mg. The analysis reveals diffuse porosity,

particularly prominent in specimens with 3 mm. Porosities are notably present along the perimeters and central areas of the struts, affecting both vertical and oblique struts and so the mechanical behavior.

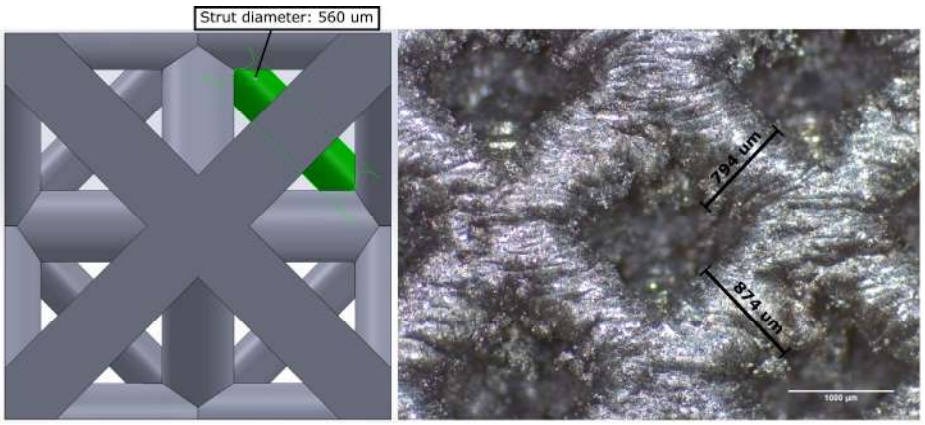

(**a**) (**b**)

Figure 15. Strut diameter analysis: (**a**) Oct-3-30 from CAD model, (**b**) Oct-3-30 from OM image 20×.

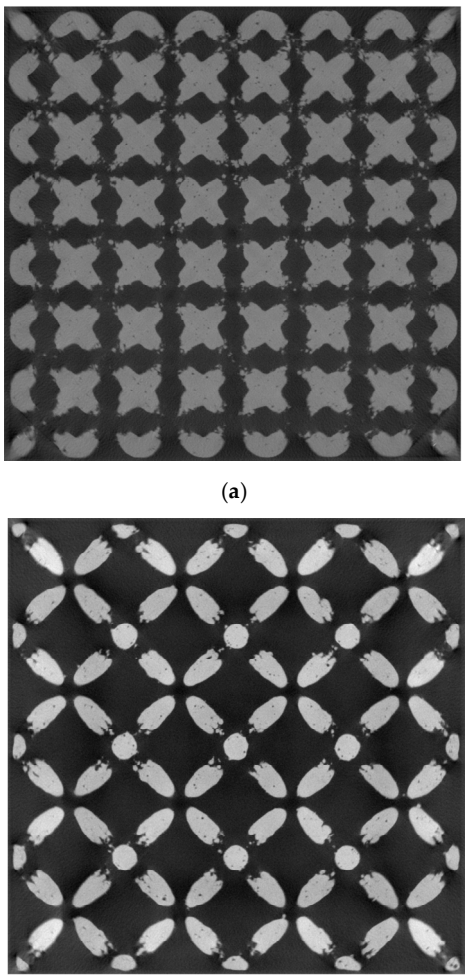

(**a**)

(**b**)

Figure 16. *Cont*.

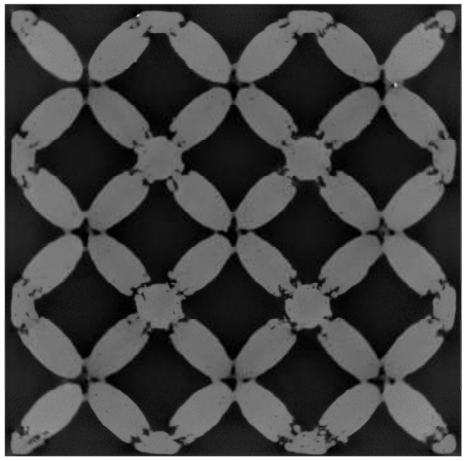

(**c**)

Figure 16. Tomography of AlSi10Mg Bccz specimens in XY plane: (**a**) Bccz-3-30, (**b**) Bccz-5-25, (**c**) Bccz-7-35.

Figure 14b focuses on the results regarding Young's modulus (E), with the GA model represented by lines and experimental data by points. The correlation between the model and experimental data is less pronounced. The correspondence is mainly observed for low-density specimens but diverges rapidly, highlighting the distinct fracture behaviors of trabecular structures compared to classical foam. This disparity is especially apparent in Bccz cells which, due to the failure of vertical struts, exhibit significant deformation before breaking and an elastic modulus lower than predicted by the model. For octet and rhombic cells, while this trend is observed at high densities, it is less pronounced. Their fracture mechanisms are more akin to those of foam, characterized by a brittle collapse of the cells. Given these observations, it becomes evident that there is a need for a new, enhanced model that can more accurately predict the mechanical behavior of these complex structures, especially at higher densities. This scenario opens new research possibilities, inviting further investigation and model development to better understand and predict the behavior of trabecular structures under various conditions.

5. Conclusions

The present study comprehensively evaluated the mechanical compression properties of AlSi10Mg lattice trusses fabricated using SLM for anti-ice system applications in aerospace. The findings underscore the exceptional adaptivity of compressive strength of these lattice structures, highlighting their suitability for customized applications requiring robust and light structures. The experimental results reveal that the mechanical properties of the lattice trusses are significantly influenced by design parameters such as cell type, cell size, and relative density.

Specifically, the research demonstrates that:

1. Cell size and type: Smaller cell sizes (3 mm) and octet-truss structures exhibit superior Young's modulus compared to larger cell sizes (5 and 7 mm) and other cell geometries (BCCZ and rhombic dodecahedron). The octet truss, characterized by shorter beam lengths, outperforms other structures due to its efficient load distribution.
2. Relative density: There is a linear relationship between relative density and all measured mechanical properties, with higher densities enhancing Young's modulus, maximum stress, and yield stress. This correlation is consistent with the Gibson–Ashby model for low-density foams, though deviations are observed at higher densities due to manufacturing and design complexities.
3. Failure mechanisms: The failure mechanisms vary with cell geometry, with stretching-dominated structures (BCCZ) showing distinct failure patterns compared to bending-

dominated structures (rhombic dodecahedron and octet truss). These differences highlight the importance of considering cell geometry in design optimization.

The study's integration of a DOE approach facilitated a nuanced understanding of how these variables interact, offering valuable insights for optimizing lattice-truss designs for specific applications. The alignment of experimental data with the Gibson–Ashby model for lower-density structures reinforces the model's applicability in predicting mechanical behavior, although the need for refined models at higher densities is evident.

Author Contributions: Conceptualization, C.G.F. and S.V.; methodology, C.G.F. and S.V.; software, S.V.; validation, C.G.F. and S.V.; formal analysis, C.G.F.; investigation, C.G.F. and S.V.; resources, C.G.F.; data curation, C.G.F. and S.V.; writing—original draft preparation, C.G.F. and S.V.; writing—review and editing, C.G.F. and S.V.; visualization, C.G.F.; supervision, P.M.; project administration, P.M.; funding acquisition, P.M. All authors have read and agreed to the published version of the manuscript.

Funding: This research received no external funding.

Data Availability Statement: The original contributions presented in the study are included in the article, further inquiries can be directed to the corresponding author/s.

Acknowledgments: The authors wish to thank all the technicians of the Mechanical Laboratory of the DIMEAS Department of Politecnico di Torino for their competence, availability and professionality.

Conflicts of Interest: The author Sara Varetti was employed by the Leonardo Labs. All authors declare that the research was conducted in the absence of any commercial or financial relationships that could be construed as a potential conflict of interest.

Appendix A. Elementary Unit Cells Drawing

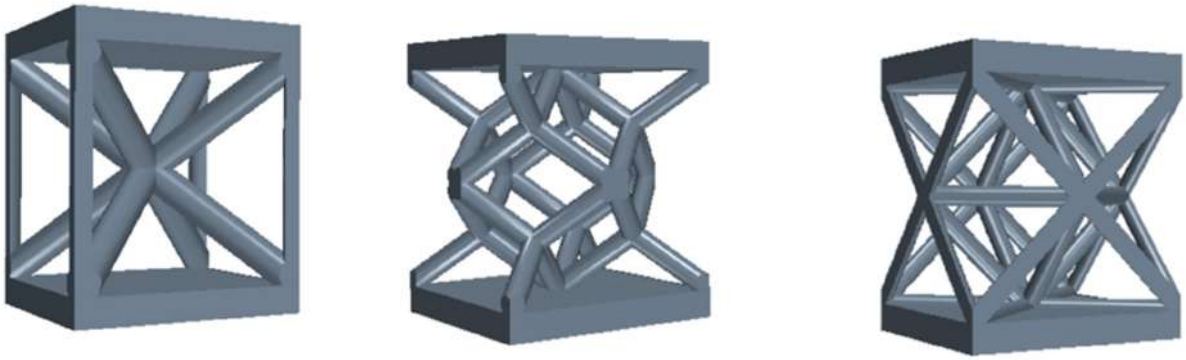

(**a**) (**b**) (**c**)

Figure A1. Elementary unit cell drawings: (**a**) Bccz model; (**b**) rhombic model; (**c**) octet model.

Appendix B. Experimental Collected Results

Table A1. Experimental results of compression tests.* No data available to this specimen due to test execution failure.

Cell Type	Cell Size	Relative Density	Sigma Max [MPa]	Sigma 02 [MPa]	Young's Modulus [MPa]
Bccz	3	25	95	48	2954
Bccz	3	30	116	59	3927
Bccz	3	35	149	77	4315
Bccz	5	25	25	15	1322
Bccz	5	30	42	25	1579
Bccz	5	35	57	31	2011

Table A1. *Cont.*

Cell Type	Cell Size	Relative Density	Sigma Max [MPa]	Sigma 02 [MPa]	Young's Modulus [MPa]
Bccz	7	25	32	18	1491
Bccz	7	30	44	24	1822
Bccz	7	35	59	32	2273
Rhombic	3	25	86	50	2847
Rhombic	3	30	108	72	4009
Rhombic	3	35	137	76	4840
Rhombic	5	25	19	15	1046
Rhombic	5	30	29	21	1522
Rhombic	5	35	42	30	2059
Rhombic	7	25	18	15	955
Rhombic	7	30	28	22	1403
Rhombic	7	35	40	30	1845
Octet	3	25	111	61	4070
Octet	3	30	156	89	5520
Octet	3	35	161	91	5902
Octet	5	25	28	24	1610
Octet	5	30	37	27	1906
Octet	5	35	57	36	2426
Octet	7	25	29	23	1502
Octet	7	30	42	29	1732
Octet	7	35	59	36	2289
Bccz	3	25	93	44	2837
Bccz	3	30	118	55	3804
Bccz	3	35	149	70	4264
Bccz	5	25	28	17	1224
Bccz	5	30	43	26	1565
Bccz	5	35	56	30	2020
Bccz	7	25	30	20	1282
Bccz	7	30	44	25	1826
Bccz	7	35	57	28	2251
Rhombic	3	25	87	51	2823
Rhombic	3	30	104	68	4254
Rhombic	3	35	135	80	4641
Rhombic	5	25	19	15	1001
Rhombic	5	30	29	22	1526
Rhombic	5	35	40	29	2006
Rhombic	7	25	17	14	908
Rhombic	7	30	28	22	1405
Rhombic	7	35	40	31	1840
Octet	3	25	112	62	4057
Octet	3	30	*	*	*
Octet	3	35	160	84	7321
Octet	5	25	28	23	1599
Octet	5	30	41	30	2011
Octet	5	35	56	36	2396
Octet	7	25	28	23	1507
Octet	7	30	42	28	1787
Octet	7	35	58	36	2240
Bccz	3	25	97	47	3000
Bccz	3	30	118	61	4821
Bccz	3	35	144	71	4224
Bccz	5	25	27	16	1233
Bccz	5	30	43	25	1707
Bccz	5	35	56	30	2018
Bccz	7	25	32	18	1626
Bccz	7	30	41	32	1337
Bccz	7	35	58	33	2219

Table A1. *Cont.*

Cell Type	Cell Size	Relative Density	Sigma Max [MPa]	Sigma 02 [MPa]	Young's Modulus [MPa]
Rhombic	3	25	86	52	2853
Rhombic	3	30	106	78	3464
Rhombic	3	35	135	89	4973
Rhombic	5	25	19	15	1096
Rhombic	5	30	29	22	1610
Rhombic	5	35	42	30	2090
Rhombic	7	25	18	15	1008
Rhombic	7	30	28	23	1440
Rhombic	7	35	41	31	1899
Octet	3	25	107	72	3747
Octet	3	30	*	*	*
Octet	3	35	*	*	*
Octet	5	25	29	22	1741
Octet	5	30	36	27	1922
Octet	5	35	53	35	2321
Octet	7	25	31	23	1595
Octet	7	30	42	29	1691
Octet	7	35	58	37	2260

References

1. Masiol, M.; Harrison, R.M. Aircraft engine exhaust emissions and other airport-related contributions to ambient air pollution: A review. *Atmos. Environ.* **2014**, *95*, 409–455. [CrossRef] [PubMed]
2. Baxter, G. Assessing the Carbon Footprint and Carbon Mitigation Measures of a Major Full-Service Network Airline: A Case Study of Singapore Airlines. *Int. J. Environ. Agric. Biotechnol.* **2022**, *7*, 81–107. [CrossRef]
3. Kloewer, M.; Allen, M.R.; Lee, D.S.; Proud, S.R.; Gallagher, L.; Skowron, A. Quantifying aviation's contribution to global warming. *Environ. Res. Lett.* **2021**, *16*, 104027. [CrossRef]
4. Ryley, T.; Baumeister, S.; Coulter, L. Climate change influences on aviation: A literature review. *Transp. Policy* **2020**, *92*, 55–64. [CrossRef]
5. Afonso, F.; Sohst, M.; Diogo, C.M.; Rodrigues, S.S.; Ferreira, A.; Ribeiro, I.; Marques, R.; Rego, F.F.; Sohouli, A.; Portugal-Pereira, J.; et al. Strategies towards a more sustainable aviation: A systematic review. *Prog. Aerosp. Sci.* **2023**, *137*, 100878. [CrossRef]
6. Dessens, O.; Köhler, M.O.; Rogers, H.L.; Jones, R.L.; Pyle, J.A. Aviation and climate change. *Transp. Policy* **2014**, *34*, 14–20. [CrossRef]
7. Gössling, S.; Humpe, A. The global scale, distribution and growth of aviation: Implications for climate change. *Glob. Environ. Chang.* **2020**, *65*, 102194. [CrossRef] [PubMed]
8. Zhang, X.; Liang, E. Metal additive manufacturing in aircraft: Current application, opportunities and challenges. *IOP Conf. Ser. Mater. Sci. Eng.* **2019**, *493*, 012032. [CrossRef]
9. Ferro, C.; Grassi, R.; Seclì, C.; Maggiore, P. Additive Manufacturing Offers New Opportunities in UAV Research. *Procedia CIRP* **2016**, *41*, 1004–1010. [CrossRef]
10. Petrovic, V.; Haro, J.V.; Jordá, O.; Delgado, J.; Blasco, J.R.; Portolés, L. Additive Layer Manufacturing: State of the art in industrial applications through case studies. *Int. J. Prod. Res.* **2011**, *49*, 1061–1079. [CrossRef]
11. Noronha, J.; Qian, M.; Leary, M.; Kyriakou, E.; Brandt, M. Hollow-walled lattice materials by additive manufacturing: Design, manufacture, properties, applications and challenges. *Curr. Opin. Solid State Mater. Sci.* **2021**, *25*, 5. [CrossRef]
12. Deckers, J. Additive manufacturing of ceramics: A review. *J. Ceram. Sci. Technol.* **2014**, *2014*, 245–260. [CrossRef]
13. Blakey-Milner, B.; Gradl, P.; Snedden, G.; Brooks, M.; Pitot, J.; Lopez, E.; Leary, M.; Berto, F.; du Plessis, A. Metal additive manufacturing in aerospace: A review. *Mater. Des.* **2021**, *209*, 110008. [CrossRef]
14. Udroiu, R. Applications of Additive Manufacturing Technologies for Aerodynamic Tests. *Acad. J. Manuf. Eng.* **2010**, *8*, 3.
15. Hao, L.; Raymont, D.; Yan, C.; Hussein, A.; Young, P. Design and additive manufacturing of cellular lattice structures. *Innov. Dev. Virtual Phys. Prototyp.* **2011**, *2016*, 249–254. [CrossRef]
16. Mclaren, D. Thermal Anti-Icing System for Aircraft. US Patent 5011098, 30 December 1988.
17. Ferro, C.; Varetti, S.; Maggiore, P.; Lombardi, M.; Biamino, S.; Manfredi, D.; Calignano, F. Design and characterization of trabecular structures for an anti-icing sandwich panel produced by additive manufacturing. *J. Sandw. Struct. Mater.* **2018**, *22*, 1111–1131. [CrossRef]
18. Ferro, C.G.; Varetti, S.; De Pasquale, G.; Maggiore, P. Lattice structured impact absorber with embedded anti-icing system for aircraft wings fabricated with additive SLM process. *Mater. Today Commun.* **2018**, *15*, 185–189. [CrossRef]
19. Vacca, A.P. 180 Main Wing Anti-Ice System: Analysis and Improvements. 2013. Available online: http://www.dicat.unige.it/bottaro/Presentation%20group/Tesi_Vacca.pdf (accessed on 30 May 2024).

20. Maggiore, P.; Ferro, C.G.; Varetti, S.; Vitti, F. Thermal Anti Ice System Integrated in the Structure and Method for Its Fabrication. 102016000098196. 2016. Available online: https://patents.google.com/patent/US20200031479A1/en (accessed on 30 May 2024).
21. Ferro, C.G. Multidisciplinary Analysis of a Novel Anti-Icing System for a Fixed Wing UAV. 2019. Available online: https://iris.polito.it/handle/11583/2742536 (accessed on 30 May 2024).
22. Bici, M.; Brischetto, S.; Campana, F.; Ferro, C.G.; Seclì, C.; Varetti, S.; Maggiore, P.; Mazza, A. Development of a multifunctional panel for aerospace use through SLM additive manufacturing. *Procedia CIRP* **2018**, *67*, 215–220. [CrossRef]
23. Ferro, C.G.; Varetti, S.; Maggiore, P. Experimental Evaluation on Fatigue Strength of Lattice Structures of AlSi10Mg Fabricated by AM for an Innovative Aerospace Anti-Ice System. *Aerospace* **2023**, *10*, 400. [CrossRef]
24. Ferro, C.G.; Pietrangelo, F.; Maggiore, P. Heat exchange performance evaluation inside a lattice panel using CFD analysis for an innovative aerospace anti-icing system. *Aerosp. Sci. Technol.* **2023**, *141*, 108565. [CrossRef]
25. Mahmoud, D.; Elbestawi, M.A. Lattice structures and functionally graded materials applications in additive manufacturing of orthopedic implants: A review. *J. Manuf. Mater. Process.* **2017**, *1*, 13. [CrossRef]
26. Chen, L.-Y.; Liang, S.-X.; Liu, Y.; Zhang, L.-C. Additive manufacturing of metallic lattice structures: Unconstrained design, accurate fabrication, fascinated performances, and challenges. *Mater. Sci. Eng. R. Rep.* **2021**, *146*, 100648. [CrossRef]
27. Hasib, H.; Rennie, A.; Burns, N.; Geekie, L. Non-stochastic lattice structures for novel filter applications fabricated via additive manufacturing. In Proceedings of the Conference: The Filtration Society 50th Anniversary International Conference and Exhibition, Chester, UK, 13–14 November 2014.
28. Seharing, A.; Azman, A.H.; Abdullah, S. A review on integration of lightweight gradient lattice structures in additive manufacturing parts. *Adv. Mech. Eng.* **2020**, *12*, 168781402091695. [CrossRef]
29. Zargarian, A.; Esfahanian, M.; Kadkhodapour, J.; Ziaei-Rad, S. Numerical simulation of the fatigue behavior of additive manufactured titanium porous lattice structures. *Mater. Sci. Eng. C* **2016**, *60*, 339–347. [CrossRef] [PubMed]
30. Dong, G.; Tang, Y.; Zhao, Y.F. A survey of modeling of lattice structures fabricated by additive manufacturing. *J. Mech. Des. Trans. ASME* **2017**, *139*, 100906. [CrossRef]
31. Tancogne-Dejean, T.; Spierings, A.B.; Mohr, D. Additively-manufactured metallic micro-lattice materials for high specific energy absorption under static and dynamic loading. *Acta Mater.* **2016**, *116*, 14–28. [CrossRef]
32. Mantovani, S.; Giacalone, M.; Merulla, A.; Bassoli, E.; Defanti, S. Effective Mechanical Properties of AlSi7Mg Additively Manufactured Cubic Lattice Structures. *3D Print. Addit. Manuf.* **2022**, *9*, 326–336. [CrossRef] [PubMed]
33. Xiao, L.; Xu, X.; Feng, G.; Li, S.; Song, W.; Jiang, Z. Compressive performance and energy absorption of additively manufactured metallic hybrid lattice structures. *Int. J. Mech. Sci.* **2022**, *219*, 107093. [CrossRef]
34. Li, D.; Qin, R.; Chen, B.; Zhou, J. Analysis of mechanical properties of lattice structures with stochastic geometric defects in additive manufacturing. *Mater. Sci. Eng. A* **2021**, *822*, 141666. [CrossRef]
35. Ueno, A.; Guo, H.; Moritoyo, R.; Takezawa, A.; Kitamura, M. Lemperature distribution design of functionally graded structure based on lattice volume fraction distribution optimization and metal additive manufacturing. *Seimitsu Kogaku Kaishi/J. Jpn. Soc. Precis. Eng.* **2021**, *87*, 827–833. [CrossRef]
36. Raž, K.; Chval, Z.; Santos, R. Development of a Computational Model of Lattice Structure. *MATEC Web Conf.* **2022**, *357*, 02012. [CrossRef]
37. Lozanovski, B.; Leary, M.; Tran, P.; Shidid, D.; Qian, M.; Choong, P.; Brandt, M. Computational modelling of strut defects in SLM manufactured lattice structures. *Mater. Des.* **2019**, *171*, 107671. [CrossRef]
38. Arabnejad, S.; Pasini, D. Mechanical properties of lattice materials via asymptotic homogenization and comparison with alternative homogenization methods. *Int. J. Mech. Sci.* **2013**, *77*, 249–262. [CrossRef]
39. Herrnböck, L.; Steinmann, P. Homogenization of fully nonlinear rod lattice structures: On the size of the RVE and micro structural instabilities. *Comput. Mech.* **2022**, *69*, 947–964. [CrossRef]
40. PBarclay, L.; Zhang, D.Z. A combined ensemble-volume average homogenization method for lattice structures with defects under dynamic and static loading. *Comput. Mater. Sci.* **2023**, *228*, 112357. [CrossRef]
41. Liu, H.; Long, L. Equivalent homogenization design method for stretching-bending hybrid lattice structures. *J. Mech. Sci. Technol.* **2023**, *37*, 4169–4178. [CrossRef]
42. Huang, L.; Yuan, H.; Zhao, H. An FEM-based homogenization method for orthogonal lattice metamaterials within micropolar elasticity. *Int. J. Mech. Sci.* **2023**, *238*, 107836. [CrossRef]
43. Somnic, J.; Jo, B.W. Status and Challenges in Homogenization Methods for Lattice Materials. *Materials* **2022**, *15*, 605. [CrossRef]
44. Somnic, J.; Jo, B.W. Homogenization Methods of Lattice Materials. *Encyclopedia* **2022**, *2*, 72. [CrossRef]
45. Beaver, R.J. Design and Analysis of Experiments-Montgomery, DC. International Biometric SOC 808 17th ST NW SUITE 200, Washington, DC 20006-3910. 1977. Available online: https://www.researchgate.net/profile/Farshad-Fattahi/post/Need-the-procedure-for-critical-limit-fixation/attachment/59d6459179197b80779a0aa7/AS:453901993418752@1485230076186/download/Douglas-C.-Montgomery-Design-and-Analysis-of-Experiments-Wiley-2012.pdf (accessed on 30 May 2024).
46. Montgomery, D.C. *Design and Analysis of Experiments*; Jojn Wiley & Sons, Inc.: Tucson, AZ, USA, 2017; p. 684.
47. SLM Solutions Group AG. SLM®500. The High Power Machine for Metal Additive Manufacturing. Available online: https://www.slm-solutions.com/en/products-and-solutions/machines/slm-500/ (accessed on 30 May 2024).

48. Latture, R.M.; Rodriguez, R.X.; Holmes, L.R.; Zok, F.W. Effects of nodal fillets and external boundaries on compressive response of an octet truss. *Acta Mater.* **2018**, *149*, 78–87. [CrossRef]
49. EOS GmbH—Electro Optical Systems. *Material Data Sheet: EOS Aluminium AlSi10Mg*; EOS GmbH: Temple, TX, USA, 2014; Volume 49, pp. 1–5.